

## Research Article

# Polarized Uniform Linear Array System: Beam Radiation Pattern, Beamforming Diversity Order, and Channel Capacity

Xin Su<sup>1</sup> and KyungHi Chang<sup>2</sup>

<sup>1</sup>Program in IT & Media Convergence Studies, Inha University, Incheon 402-751, Republic of Korea

<sup>2</sup>Electronic Engineering Department, Inha University, Incheon 402-751, Republic of Korea

Correspondence should be addressed to KyungHi Chang; khchang@inha.ac.kr

Received 22 October 2014; Accepted 20 February 2015

Academic Editor: Massimiliano Simeoni

Copyright © 2015 X. Su and K. Chang. This is an open access article distributed under the Creative Commons Attribution License, which permits unrestricted use, distribution, and reproduction in any medium, provided the original work is properly cited.

There have been many studies regarding antenna polarization; however, there have been few publications on the analysis of the channel capacity for polarized antenna systems using the beamforming technique. According to Chung et al., the channel capacity is determined by the density of scatterers and the transmission power, which is obtained based on the assumption that scatterers are uniformly distributed on a 3D spherical scattering model. However, it contradicts the practical scenario, where scatterers may not be uniformly distributed under outdoor environment, and lacks the consideration of fading channel gain. In this study, we derive the channel capacity of polarized uniform linear array (PULA) systems using the beamforming technique in a practical scattering environment. The results show that, for PULA systems, the channel capacity, which is boosted by beamforming diversity, can be determined using the channel gain, beam radiation pattern, and beamforming diversity order (BDO), where the BDO is dependent on the antenna characteristics and array configurations.

## 1. Introduction

Recently, there has been a gradual increase in the demand for polarized antenna systems, especially for 5G networks. This is mainly because antenna polarization is an important parameter employed for the design of space-limited wireless devices [1, 2]. Several techniques such as space-time diversity, multiplexing, and array processing can be exploited in order to boost the system throughput for polarized antennas. Thus, many published research articles as well as ongoing projects have focused on antenna polarization [3–5]. However, there have been few reports on the analysis of the channel capacity for polarized antenna systems using the beamforming technique. In [6], the channel capacity is known to be determined by the density of scatterers and the transmission power instead of other system parameters. This is based on the compact uniform linear array (ULA) and assumes that scatterers are uniformly distributed on a 3D spherical scattering model. However, in practical scenarios, the scatterers may not be uniformly distributed, especially in outdoor environments. In addition, [6] does not consider the fading channel, which

is important when obtaining the channel capacity in [7, 8]. In this study, we obtain the channel capacity of polarized ULA (PULA) systems using the beamforming technique in a practical scattering environment. Our results indicate that, for PULA systems, the channel capacity, which is boosted by beamforming diversity, is determined mainly by the channel gain, beam radiation pattern, and beamforming diversity order (BDO).

In this paper, the beam radiation pattern (including the beamwidth, the number of lobes, and the radiation gain of the beam) of conventional ULA systems is described based on the antenna characteristics and array configurations (i.e., dipole antennas with different lengths, the number of array elements, and the array element spacing). And we characterize the beam radiation pattern for PULA systems in both 2D and 3D forms, where the dipole antenna-based PULA is shown to have a higher beam radiation gain compared with isotropic antenna-based systems. The BDO, which is defined with respect to the number of beam lobes generated by the transceiver, is obtained under different transmission scenarios by considering the line-of-sight (LOS) component

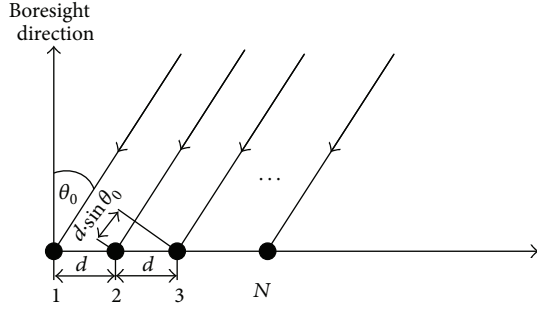


FIGURE 1: Configuration of the conventional ULA.

and scattering environments. In addition, it is dependent on the antenna characteristics and array configurations and has been shown to be linearly proportional to the number of array elements and array element spacing.

The remainder of this paper is organized as follows. In Section 2, we analyze the conventional ULA, while the beam radiation patterns of the PULA in both 2D and 3D forms are presented in Section 3. In Section 4, we introduce the BDO concept, and in Section 5 we discuss the channel capacity of PULA systems. Finally, we conclude the paper in Section 6.

## 2. Feature Analysis of Conventional ULA

**2.1. Array Factor.** Figure 1 illustrates a conventional ULA, where  $\theta_0$  denotes the signal incidence angle shifted from the boresight direction (the antenna boresight is the axis vertical to the orientation of the array alignment [9]),  $d$  represents the array element spacing, and  $N$  is the number of array elements. The array factor  $F(\theta)$ , which represents the far-field radiation of an isotropic ULA system [10], can be expressed in terms of the inner product of the weighting vector and array propagation vector as follows:

$$F(\theta) = \mathbf{w} \cdot \mathbf{v}. \quad (1)$$

The weighting vector is given as

$$\mathbf{w} = [w_1 \ w_2 \ \dots \ w_N], \quad (2a)$$

and the array propagation vector is given as

$$\mathbf{v} = [1, e^{j(2\pi d/\lambda) \sin \theta}, \dots, e^{j(N-1)(2\pi d/\lambda) \sin \theta}]^T, \quad (2b)$$

where  $\lambda$  denotes the signal wavelength. If we use the weighting vector to adjust a beam with a specific angle (shifted from the boresight direction) of  $\theta_0$  and use the array spacing factor  $\varepsilon$  to describe the array configuration, that is,  $d = \lambda/\varepsilon$ , the array factor can be further expressed as

$$F(\theta) = \sum_{n=1}^N e^{j(n-1)(2\pi/\varepsilon)(\sin \theta - \sin \theta_0)}. \quad (3)$$

Based on the derivation in Appendix A, the normalized  $F(\theta)$  is obtained as

$$F(\theta) = \begin{cases} \frac{\sin((\pi N/\varepsilon)(\sin \theta - \sin \theta_0))}{N \cdot \sin((\pi/\varepsilon)(\sin \theta - \sin \theta_0))}, & \theta \neq \theta_0 \\ 1, & \theta = \theta_0. \end{cases} \quad (4)$$

Because  $-2 \leq \sin \theta - \sin \theta_0 \leq 2$  and  $\varepsilon \geq 2$  are often used to avoid the array aliasing problem [11],  $F(\theta)$  then approximates to the sinc function as

$$F(\theta) \approx \begin{cases} \text{sinc}\left(\frac{\pi N}{\varepsilon}(\sin \theta - \sin \theta_0)\right), & \theta \neq \theta_0 \\ 1, & \theta = \theta_0. \end{cases} \quad (5)$$

**2.2. Off-Boresight Angle.** As discussed in [9], the beamwidth is increased significantly when the beam steers to an angle far off the boresight direction, such as the case when  $\theta_0$  reaches  $90^\circ$ . Note that the beamwidth generally refers to the width of the main-lobe of a beam. To illustrate this, we obtain the half power beamwidth (HPBW) by setting  $F(\theta) = \sqrt{1/2}$ . In addition, from  $\text{sinc}(1.391) \approx \sqrt{1/2}$ , the HPBW can be given as

$$\text{HPBW} \approx 2 \left| \arcsin\left(1.391 \frac{\varepsilon}{\pi N} + \sin \theta_0\right) \right|. \quad (6)$$

This illustrates that the beamwidth is inversely proportional to the number of array elements  $N$  and array element spacing  $d$  but is directly proportional to the off-boresight angle  $\theta_0$ . Figure 2 shows HPBW examples of isotropic ULA systems that were obtained by varying  $\theta_0$  for three different angles, that is,  $\theta_0 = 0^\circ, 45^\circ,$  and  $90^\circ$ . The figure shows that the HPBW extends about four times when  $\theta_0$  changes from  $0^\circ$  to  $90^\circ$ . Note that, in this illustration, we set  $N = 8$  and  $\varepsilon = 2$  and the boresight direction along the horizontal axis. To focus the beamwidth when there is a large off-boresight angle effect, [9] proposes a *sensor delay line*-based array system, which can effectively prevent the larger off-boresight angle effect by increasing the dimensions of the array system.

**2.3. Number of Lobes for a Beam.** We previously discussed the beamwidth, which is affected by the number of array elements, the array element spacing, and the off-boresight angle. In this section, we analyze the relationship between these factors and the number of lobes present in a beam. In the case where relays from different directions are used to contribute space diversity in an effort to boost the capacity of a ULA system [12], all of the lobes of a beam need to be considered as the BDO, which is eventually used to derive the channel capacity.

According to (4), there are zero values at  $\sin \theta = \pm(\varepsilon \cdot n/N) + \sin \theta_0$ , where  $n = 0, \dots, N-1$  and  $\theta \in (0, \pi)$ . Therefore, the lobe-widths of the ULA beam are given by

$$W_n = \left\{ \theta : \pm \frac{\varepsilon n}{N} + \sin \theta_0 \leq \sin \theta < \pm \frac{\varepsilon(n+1)}{N} + \sin \theta_0 \right\}. \quad (7)$$

Because each lobe has two zero points and there are total  $2N\varepsilon^{-1}$  zero points at  $\theta \in (0, \pi)$ , we can find  $(2N\varepsilon^{-1} - 1)$  lobes. Due to the symmetrical beam pattern of ULAs, the overall number of lobes is given as  $(4N\varepsilon^{-1} - 2)$ , which is unrelated to the off-boresight angle  $\theta_0$ . Figure 3 depicts the number of lobes when  $N$  is incremented with  $\varepsilon = 2$ , where the number of lobes can be easily observed as 6, 14, 30, and 62 when  $N$  equals

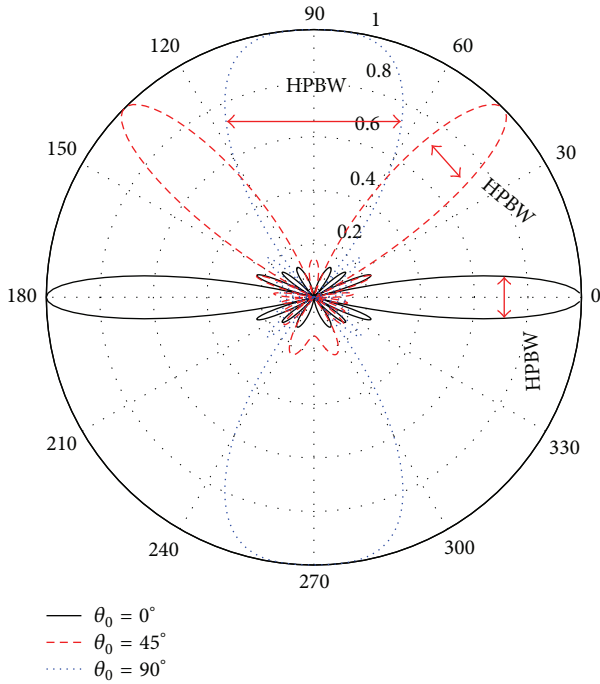


FIGURE 2: Illustration of the off-boresight angle effect.

4, 8, 16, and 32, respectively. Based on the above analysis, we can make the following proposition.

**Proposition 1.** *The beamwidth and number of lobes of a beam are relevant to the array configuration. The beamwidth is inversely proportional to the number of array elements and the array element spacing but is directly proportional to the off-boresight angle. Meanwhile, the number of lobes of a beam is proportional to the number of array elements and the array element spacing but has no relationship with the off-boresight angle.*

### 3. Beam Radiation Pattern of PULA

In this section, we discuss the beam pattern associated with the antenna characteristics, such as the use of dipole antennas, where the beamwidth and beam lobe gain are different from the case that uses the isotropic ULA.

#### 3.1. Cross-Array Beam Generation by PULA Configuration.

The dipole antenna or doublet is the most widely used class of antenna, and the radiation pattern analysis throughout this paper is based mainly on the dipole antenna. Figure 4 demonstrates a dipole antenna with a length of  $L$ .  $a(\theta, \phi, \gamma, \kappa)$  denotes the far-field radiation pattern of the dipole, where  $\gamma$  is the angle of the dipole shifted from the  $z$ -axis and  $\kappa$  is the factor used to determine the dipole length; that is,  $L = \kappa\lambda$ . The half-wavelength dipole is defined when  $\kappa = 1/2$ . Figure 5 shows our proposed orthogonal triple-polarized dipole ULA, where an array and branch (A&B) multiple antenna configuration is depicted. In other words, the PULA system is composed of several paralleled array elements,

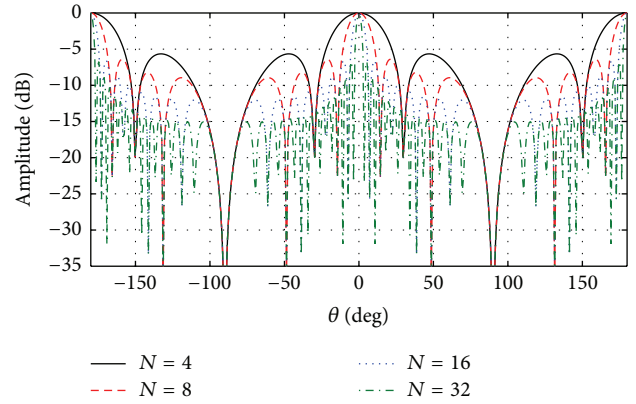
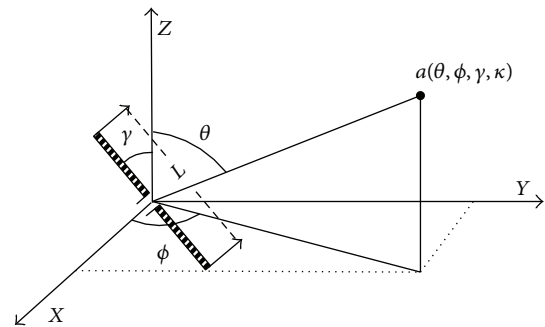

 FIGURE 3: The number of beam lobes varies with different  $N$  values.


FIGURE 4: Configuration of the dipole antenna.

and there are three orthogonal colocated branches/dipoles at each array element. Three branch sets of  $A_n B_1$ ,  $A_n B_2$ , and  $A_n B_3$  are implemented along the  $z$ -axis,  $y$ -axis, and  $x$ -axis, respectively.

Because three colocated branches at each array element are fixed with zero spacing, as shown in Figure 5, which makes the beamwidth scale up to  $360^\circ$  according to Proposition 1, the beams need to be generated by using corresponding cross-array branches rather than the colocated branches at each array element. Therefore, we can obtain three orthogonal beams generated by a PULA as follows:

- (i) The beam varied in the  $x$ - $y$  plane is generated by the set of branches of  $A_n B_1$ , where  $n = 1, 2, \dots, N$ .
- (ii) The beam varied in the  $x$ - $z$  plane is generated by the set of branches of  $A_n B_2$ .
- (iii) The beam varied in the  $y$ - $z$  plane is generated by the set of branches of  $A_n B_3$ .

**3.2. PULA Beam Radiation Pattern in 2D Form.** First, the PULA radiation pattern is analyzed in 2D form, where only two orthogonal colocated branches (vertical and horizontal) are implemented at each array element. By fixing the vertical branch along with the vertical axis when  $\gamma = 0$ , we have the

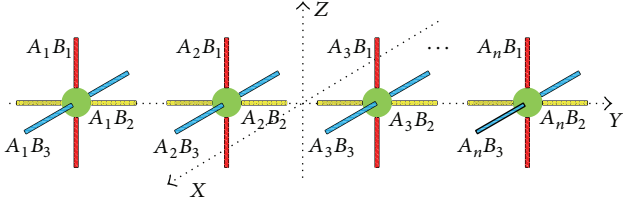


FIGURE 5: A&B multiple antenna configuration of the triple-polarized dipole ULA.

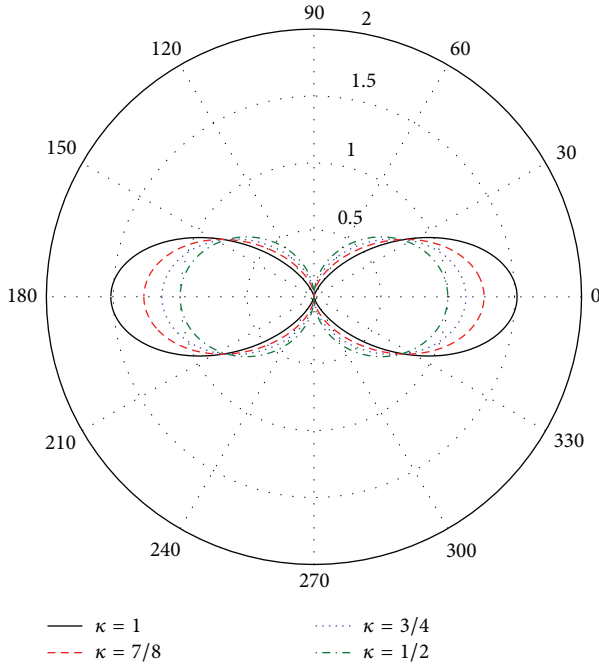


FIGURE 6: Radiation patterns of the vertical dipole in 2D form.

following: the vertical dipole radiation pattern  $a_v(\theta, \kappa)$  in 2D form (where  $\phi = 0$ ) is presented as

$$a_v(\theta, \kappa) = \frac{\cos(\pi\kappa \sin \theta) - \cos(\pi\kappa)}{\cos \theta}. \quad (8)$$

Figure 6 depicts the dipole radiation pattern of the vertical branch with  $\kappa$  different values. We observe that the dipole does not radiate in the longitudinal direction of the antenna structure and consequently has a higher gain compared with that of an isotropic antenna. In addition, the radiation pattern has a higher gain and narrower width as  $\kappa$  increased, where the case of  $\kappa = 1$  achieves the lowest angle of radiation and the highest horizontal range. Note that when  $\kappa > 1$ , the radiation pattern of the dipole does not follow the current shape in Figure 6 [13].

The radiation pattern of the colocated dipole can be easily obtained based on (8) as

$$a_h(\theta, \kappa) = \frac{\cos(\pi\kappa \sin(\theta - \gamma)) - \cos(\pi\kappa)}{\cos(\theta - \gamma)}, \quad (9)$$

where it is shifted by  $\gamma$  degrees and the horizontal dipole pattern is obtained as  $\gamma = 90^\circ$ . The PULA 2D beam radiation

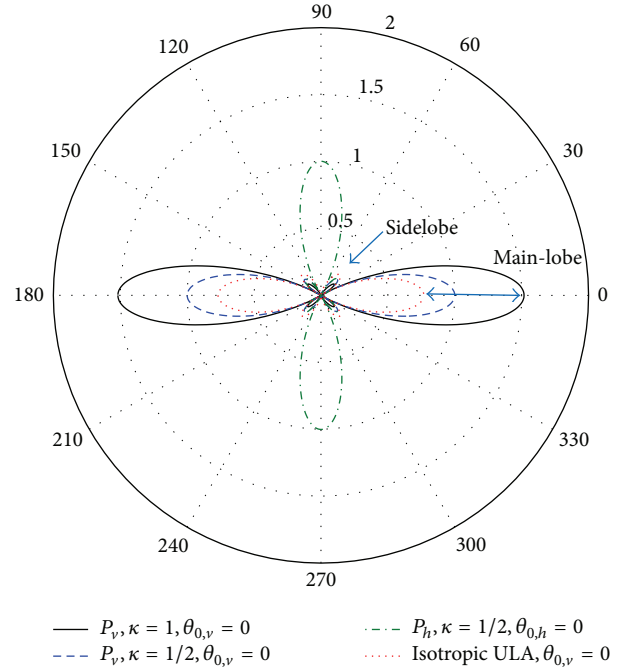


FIGURE 7: Beam radiation patterns of the PULA in 2D form.

pattern is expressed by multiplying the array factor and the radiation pattern of a single polarized antenna. Let  $P_v(\theta, \kappa, \theta_{0,v})$  and  $P_h(\theta, \kappa, \theta_{0,h})$  denote the beam radiation patterns generated by the sets of vertical dipoles and horizontal dipoles, respectively. We have

$$\begin{aligned} P_v(\theta, \kappa, \theta_{0,v}) &= a_v(\theta, \kappa) \frac{\sin((\pi N/\epsilon)(\sin \theta - \sin \theta_{0,v}))}{N \cdot \sin((\pi/\epsilon)(\sin \theta - \sin \theta_{0,v}))}, \\ P_h(\theta, \kappa, \theta_{0,h}) &= a_h(\theta, \kappa) \frac{\sin((\pi N/\epsilon)(\cos \theta - \sin \theta_{0,h}))}{N \cdot \sin((\pi/\epsilon)(\cos \theta - \sin \theta_{0,h}))}, \end{aligned} \quad (10)$$

where  $\theta_{0,v}$  and  $\theta_{0,h}$  are the off-boresight angles corresponding to the sets of vertical branches and horizontal branches, respectively.

Figure 7 is drawn when  $N = 4$  and  $\epsilon = 2$ . We observe that the beam radiation patterns generated by the sets of vertical dipoles and horizontal dipoles have a  $90^\circ$  rotation. The beamforming gain can be extended by increasing the dipole length. However, the trade-off regarding the antenna size needs to be considered in the antenna design. The 2D beam radiation pattern for an isotropic ULA is also given in Figure 7 for comparison purposes, where it has a larger sidelobe and smaller main-lobe pattern compared with the dipole-based array system [14]. This is mainly because the dipole does not radiate in the longitudinal direction of the antenna structure and maintains a higher radiation gain compared with that of the isotropic antenna.

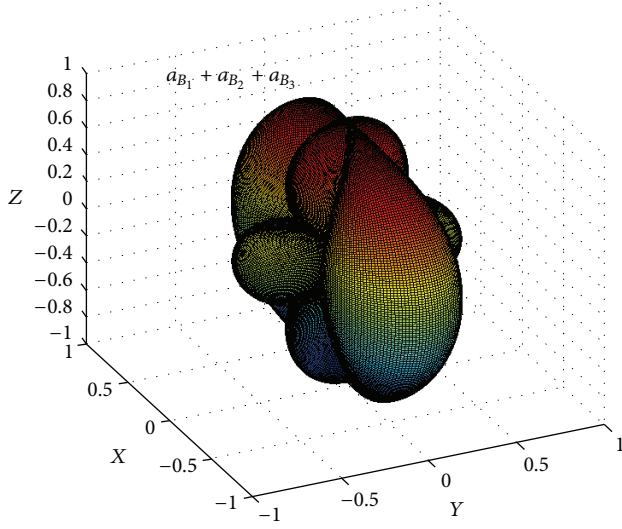


FIGURE 8: Radiation patterns of the triple-polarized half-wavelength dipole in 3D form.

**3.3. PULA Beam Radiation Pattern in 3D Form.** In [3], the 3D dipole radiation pattern is found to have a donut shape. In addition, the 3D radiation pattern of the dual-polarized half-wavelength dipole was investigated in [4, 15] with different inclination angles of  $\gamma$ , for example,  $0^\circ$ ,  $45^\circ$ , and  $90^\circ$ . In this paper, we further obtain the 3D radiation pattern for a triple-polarized system, where three colocated dipoles ( $B_1$ ,  $B_2$ , and  $B_3$ ) are deployed along the  $z$ -axis,  $y$ -axis, and  $x$ -axis, respectively. The formulae for the radiation pattern derived based on (31) in [4] for these three colocated dipoles are given as

$$\begin{aligned} a_{B_1}(\theta, \phi) &= \cos \theta \cos \phi \frac{\cos((\pi/2) \sin \theta \cos \phi)}{1 - \sin^2 \theta \cos^2 \phi}, \\ a_{B_2}(\theta, \phi) &= \sin \theta \cos \phi \frac{\cos((\pi/2) \sin \theta \cos \phi)}{1 - \sin^2 \theta \cos^2 \phi}, \\ a_{B_3}(\theta, \phi) &= \sin \phi \frac{\cos((\pi/2) \sin \theta \cos \phi)}{1 - \sin^2 \theta \cos^2 \phi}. \end{aligned} \quad (11)$$

Based on (11) the radiation patterns of triple-polarized half-wavelength dipoles are plotted in Figure 8, where the three patterns affect each other and the donut radiation shape of the dipole antenna is reshaped due to the presence of colocated dipoles.

Similar to the 2D case, the PULA 3D beam radiation pattern was also obtained by multiplying the array factor and radiation pattern of a single polarized antenna. Let  $P_{B_1}(\theta, \phi, \theta_{0,1})$ ,  $P_{B_2}(\theta, \phi, \theta_{0,2})$ , and  $P_{B_3}(\theta, \phi, \theta_{0,3})$  represent the

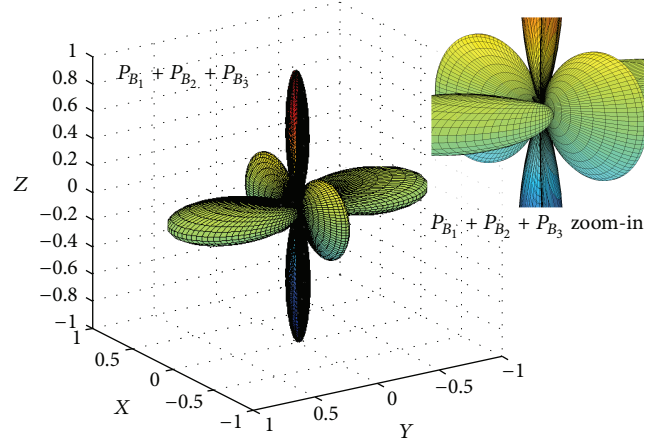


FIGURE 9: Beam radiation patterns of PULA in 3D form.

beam radiation patterns generated by the three dipole sets  $A_n B_1$ ,  $A_n B_2$ , and  $A_n B_3$ , respectively. We have

$$\begin{aligned} P_{B_1}(\theta, \phi, \theta_{0,1}) &= \sum_{n=1}^N a_{B_1} \cdot e^{j(n-1)(2\pi/\epsilon)(\sin \theta - \sin \theta_{0,1})} \\ &= a_{B_1} \frac{\sin((\pi N/\epsilon)(\sin \theta - \sin \theta_{0,1}))}{N \cdot \sin((\pi/\epsilon)(\sin \theta - \sin \theta_{0,1}))}, \\ P_{B_2}(\theta, \phi, \theta_{0,2}) &= \sum_{n=1}^N a_{B_2} \cdot e^{j(n-1)(2\pi/\epsilon)(\sin \phi - \sin \theta_{0,2})} \\ &= a_{B_2} \frac{\sin((\pi N/\epsilon)(\sin \phi - \sin \theta_{0,2}))}{N \cdot \sin((\pi/\epsilon)(\sin \phi - \sin \theta_{0,2}))}, \\ P_{B_3}(\theta, \phi, \theta_{0,3}) &= \sum_{n=1}^N a_{B_3} \cdot e^{j(n-1)(2\pi/\epsilon)(\sin(\pi/2 - \phi) - \sin \theta_{0,3})} \\ &= a_{B_3} \frac{\sin((\pi N/\epsilon)(\cos \phi - \sin \theta_{0,3}))}{N \cdot \sin((\pi/\epsilon)(\cos \phi - \sin \theta_{0,3}))}, \end{aligned} \quad (12)$$

where  $\theta_{0,1}$ ,  $\theta_{0,2}$ , and  $\theta_{0,3}$  are the off-boresight angles corresponding to  $A_n B_1$ ,  $A_n B_2$ , and  $A_n B_3$ , respectively.

By setting  $N = 4$  and  $\epsilon = 2$ , we plot the beam radiation pattern of a PULA in 3D form, as illustrated by Figure 9. We can see that the main-lobe petal of each beam has a shell shape, which is mainly formed by the interaction of the electromagnetic fields of colocated beams.

#### 4. Beamforming Diversity Order (BDO)

In the relevant studies, for example, [16, 17], the interference reduction by beamforming is studied, where the sidelobe radiation of a beam is suppressed via the leaky wave antenna and particle swarm optimization in order to decrease the sidelobe interferences caused at neighbor cells. However, in this paper, we focus on the theoretical analysis under a perfect scenario without any interference. The radiation of sidelobes can also contribute to the SNR that enhances the

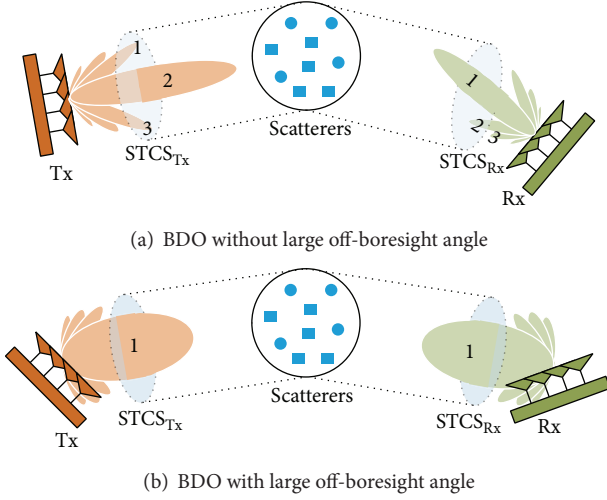


FIGURE 10: Transmission scenario with beamforming technology.

capacity, because the BDO is increased with the additional number of sidelobes. Figure 10 describes a radio transmission scenario when beamforming technology is applied at both the transmitter (Tx) and receiver (Rx). In this case, we define the signal-transmission cutting surface (STCS), which is the surface that holds the signal from the Tx to the Rx. According to Figure 10(a), three lobes are simultaneously held by the STCS at the Tx ( $STCS_{Tx}$ ), and three lobes are simultaneously held by the STCS at the Rx ( $STCS_{Rx}$ ). And we define the BDO as the multiplication of the number of lobes cut by  $STCS_{Tx}$  and  $STCS_{Rx}$ . For example, in the case of Figure 10(a), the BDO is 9. On the other hand, the BDO may decrease because of the large off-boresight angle effect, as illustrated in Figure 10(b); for example, the BDO is one where only one lobe is held by the  $STCS_{Tx}$  and  $STCS_{Rx}$ .

Practically, the scatterers are often distributed into clusters [18, 19]. A group of local scatterers within a cluster have relatively close coordinates on the sphere representing the incidence signal scattered by the roofs, walls, trees, windows, doors, and so on from a correlated direction. Meanwhile, global scatterers among different clusters have independent coordinates, which denote the incidence signal scattered from uncorrelated directions. Given a cluster of local scatterers, for the  $i$ th scatterer with a polar coordinate of  $C_i(r_i, \theta_i)$ , the signal response after scattering is given as

$$h_i(t) = A_i(t - \tau_{Tx}(C_i) - \tau_{Rx}(C_i)) \cdot \exp(-j2\pi f_c(\tau_{Tx}(C_i) + \tau_{Rx}(C_i))), \quad (13)$$

where  $\tau_{Tx}(C_i)$  is the signal propagation delay from the Tx to  $C_i$ ,  $\tau_{Rx}(C_i)$  is the signal propagation delay from  $C_i$  to the Rx, and  $f_c$  denotes the signal carrier frequency.  $A_i$  represents the channel gain and  $\exp(\cdot)$  gives the signal phase rotation after scattering. Because the local scatterers in this cluster are very close to each other, we have

$$\tau_{Tx}(C_i) + \tau_{Rx}(C_i) \approx \tau_{Tx}(C_0) + \tau_{Rx}(C_0) \quad (14)$$

for  $i = 1, \dots, I$ ,

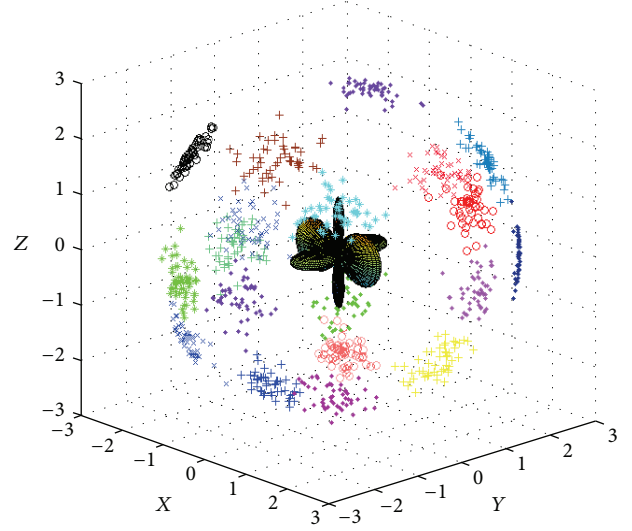


FIGURE 11: Scattering environment.

where  $C_0$  represents the coordinates of the center of gravity for the cluster. Then,  $h_0(t)$  can be used to represent the scattered signal as follows:

$$h_0 = h_i|_{C_i=C_0}. \quad (15)$$

When the scatterers in different clusters are not close to each other,  $(\tau_{Tx}(C_{0,q}) + \tau_{Rx}(C_{0,q}))$  is independent of  $(\tau_{Tx}(C_{0,q+1}) + \tau_{Rx}(C_{0,q+1}))$  for  $q = 1, \dots, Q$ , where  $C_{0,q}$  is the coordinate of the center of gravity for the  $q$ th cluster. Then, the received signal power can be denoted as

$$P(t) = \int_0^\infty \int_{\theta_{\min}}^{\theta_{\max}} |A_{0,q}(t - \tau_{Tx}(C_{0,q}) - \tau_{Rx}(C_{0,q})) \cdot \exp(-j2\pi f_c(\tau_{Tx}(C_{0,q}) + \tau_{Rx}(C_{0,q})))|^2 d\theta_{0,q} dr_{0,q}. \quad (16)$$

The fully scattered environment refers to the scattered signal coming from all directions; that is,  $\theta_{\min} = -\pi$  and  $\theta_{\max} = \pi$ , and dense urban and indoor scenarios are usually studied under such an environment. The non-fully-scattered environment is realized when  $\theta_{\min} > -\pi$  and  $\theta_{\max} < \pi$ . Most rural and remote scenarios, where wide open spaces and flat terrain fulfill the LOS conditions, are studied in this environment [20].

We assume the scenario where the Tx, which steers its main-lobe toward Rx, is located far from Rx. Consequently, the BDO at the Tx side can be assumed to be one, and the overall BDO of the system is determined only by the Rx. In addition, suppose several clusters of local scatterers are located on a sphere that encircles the Rx, as illustrated in Figure 11; we can summarize the system BDO as given by Table 1. From Table 1, we note that BDO equals the number of lobes generated by the Rx in a fully scattered scenario. In the case where the LOS component exists in a non-fully-scattered environment, the main-lobe of the Tx covers half of the surface of the sphere around the Rx. Therefore, the BDO is varied from  $2N\epsilon^{-1} - 1$  to  $4N\epsilon^{-1} - 2$ . For the case of

TABLE 1: BDO values depending on scenarios.

Scenario	BDO
LOS + NLOS (fully scattered)	$\{4N\epsilon^{-1} - 2\}_{\text{Rx}}$
NLOS (fully scattered)	$\{4N\epsilon^{-1} - 2\}_{\text{Rx}}$
LOS + NLOS (non-fully-scattered)	$\{2N\epsilon^{-1} - 1 \leq \text{BDO} \leq 4N\epsilon^{-1} - 2\}_{\text{Rx}}$
NLOS (non-fully-scattered)	$\{1 \leq \text{BDO} \leq 2N\epsilon^{-1} - 1\}_{\text{Rx}}$

the non-LOS (NLOS) in a non-fully-scattered scenario, the BDO is varied from one to  $2N\epsilon^{-1} - 1$ . Compared with the diversity order found in [3], our findings in Table 1 clearly describe the diversity order associated with the factor of the array configuration in practical scattering environments. Moreover, the fact that each lobe has two zero points was overlooked in [3].

## 5. Channel Capacity by PULA with Beamforming

For a fully scattered environment under the assumption that there is no interference, [6] derives the channel capacity for an array system as follows:

$$C = \frac{\rho \cdot \eta}{N_0} \log e [\text{bit/s}], \quad (17)$$

where  $\rho = I_s / (8(2\pi/\lambda)^2 R_s^2)$ .  $\rho$  refers to the density of the scatterers located on the 3D spherical model,  $I_s$  is the number of scatterers,  $R_s$  is the radius of the scattering sphere,  $\eta$  is the transmission power, and  $N_0$  indicates the additive noise power density. From (17), we observe that the channel capacity is only related to the scatterer density and transmission power as opposed to other system parameters. Equation (7) concludes in two ways. At first, it describes that the capacity is regardless of the system bandwidth, where a high throughput can be achieved even by a negligibly small bandwidth. And second, it shows that the capacity is irrespective of the antenna array configuration. However, the conclusions in [6] were obtained using a ULA compact antenna with  $\epsilon \gg 2$ , and based on Table 1 the diversity order thus decreases significantly. In [6], we also see that (17) is employed when the scatterers are uniformly distributed on the sphere. This is not the case practically, and the scatterers' distribution may follow the example shown in Figure 11. In addition, the fading channel gain, which is usually used to derive the channel capacity, was not considered by (7). Therefore, we provide a new method to obtain the channel capacity for PULA systems, and this method is based mainly on the fading channel gain, beam radiation pattern, and BDO.

In [7, 8], the channel capacity with Rx diversity is given by

$$C = E \left\{ \log_2 \left( 1 + |h|^2 \frac{\text{SNR}}{2} \right) \right\}, \quad (18)$$

where  $h$  denotes a gain of fading channel. Here, we define the beam lobe signal to noise power ratio (LSNR) based on the beam radiation pattern as

$$\text{LSNR}_{\hat{\theta}_k} \triangleq \frac{|P(\hat{\theta}_k, \kappa)|^2}{|n_k|^2}, \quad (19)$$

where  $k$  denotes the lobe index of the beam,  $\hat{\theta}_k$  (can be found in Appendix B) holds the condition for  $P(\theta, \kappa)$  having peak values, and  $n_k$  refers to the added noise power at the  $k$ th lobe. Based on (19), the effect of the off-boresight angle can be disregarded according to Proposition 2.

**Proposition 2.** *The off-boresight angle does not affect the lobe power but affects the lobe-width (proved by Appendix B).*

The channel capacity for a PULA system under the Rayleigh fading channel can be given as

$$C_{\text{Rayleigh}} = E \left\{ \xi \sum_{k=1}^{4N\epsilon^{-1}-2} \log_2 \left( 1 + \frac{|h_k P(\hat{\theta}_k, \kappa)|^2}{|n_k|^2} \right) \right\}, \quad (20)$$

where  $\xi = 6$  is the degree-of-freedom of the triple-polarized antenna in [3].  $h_k$  denotes a gain of fading channel corresponding to the  $k$ th lobe. Then, the capacity upper bound is found by Jensen's inequality for concave functions as follows:

$$C_{\text{Rayleigh}} \leq 2\xi \sum_{k=1}^{2N\epsilon^{-1}-1} \log_2 \left( 1 + \frac{|E\{h_k\} P(\hat{\theta}_k, \kappa)|^2}{|n_k|^2} \right). \quad (21)$$

By assuming that LOS components exist and the Rx PULA steers its main-lobes towards the LOS signal, the capacity upper bound under the Rician fading channel can be given as

$$C_{\text{Rician}} \leq \xi \log_2 \left( 1 + \frac{|E\{\sqrt{K/(K+1)}h_0 + \sqrt{1/(K+1)}h_1\} P(\hat{\theta}_1, \kappa)|^2}{|n_1|^2} \right) + \xi \log_2 \left( 1 + \frac{|E\{h_1\} P(\hat{\theta}_1, \kappa)|^2}{|n_1|^2} \right) + \xi \sum_{k=2}^{4N\epsilon^{-1}-2} \log_2 \left( 1 + \frac{|E\{h_k\} P(\hat{\theta}_k, \kappa)|^2}{|n_k|^2} \right), \quad (22)$$

where the first term contains the capacity contributed by the main-lobe that steers the LOS component ( $K$  is the Rician  $K$ -factor). The second term represents the capacity obtained by this main-lobe for the NLOS component, while the third term indicates the capacity from other lobes of the NLOS component. Note that (21) and (22) apply to the scenario

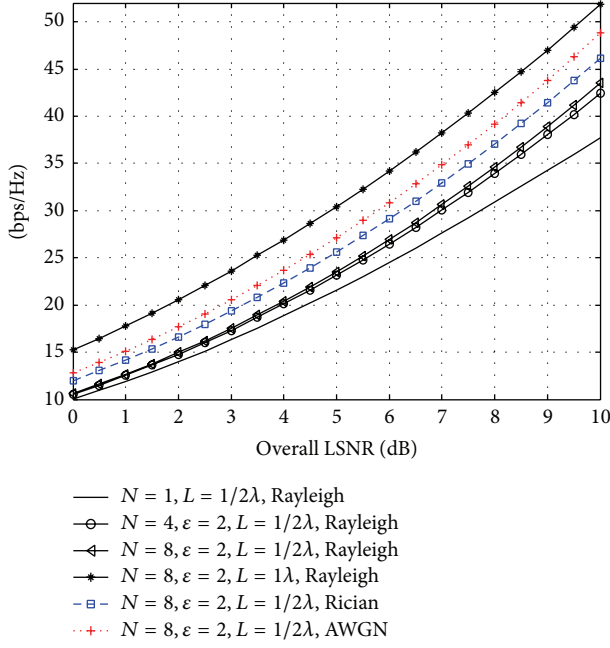


FIGURE 12: The normalized channel capacity for PULA with beamforming.

involving a fully scattered environment. In the case of a non-fully-scattered environment, the PULA capacity is decreased due to the decrement of BDO.

Figure 12 gives the normalized channel capacity for PULA with beamforming. From Figure 12, we observe that, by extending the dipole length (e.g.,  $L = 1\lambda$ ), we can effectively increase the capacity of the PULA system. This is because the radiation gain increases as  $\kappa$  increases, where the case of  $\kappa = 1$  achieves the highest gain, as discussed in Section 3. The channel capacity is also increased when more array elements are implemented (e.g.,  $N = 8$ ), and this is mainly due to the increment of the BDO. Compared with the capacity increment obtained by extending the dipole length, the capacity increment due to the BDO is small because the array factor is normalized by the number of array elements in (4). Finally, Figure 12 depicts the channel capacity under different channel models, where the AWGN has a higher capacity than in the case of fading channels. In addition, the Rician fading channel with  $K = 9$  dB can achieve a higher channel capacity compared with the Rayleigh fading channel due to the presence of the LOS component.

## 6. Conclusions

In this paper, we derive the channel capacity for PULA systems using the beamforming technique. Our results show that the channel capacity is determined mainly by three system indexes, that is, the fading channel gain, beam radiation pattern, and BDO, where the BDO is dependent on the antenna characteristics and array configurations. In contrast to conventional works, we also consider the fading channel in a practical scattering environment, and the numerical results

confirm the validity of the channel capacity obtained in this paper.

## Appendices

### A. Proof of Equation (4)

*Proof.* Multiplying  $e^{j(2\pi/\varepsilon)(\sin\theta - \sin\theta_0)}$  on both sides of (3), we have

$$F(\theta) \cdot e^{j(2\pi/\varepsilon)(\sin\theta - \sin\theta_0)} = \sum_{n=1}^N e^{j(2\pi n/\varepsilon)(\sin\theta - \sin\theta_0)}. \quad (\text{A.1})$$

Then,  $F(\theta) \cdot e^{j(2\pi/\varepsilon)(\sin\theta - \sin\theta_0)} = F(\theta) + e^{j(2\pi N/\varepsilon)(\sin\theta - \sin\theta_0)} - 1$ , and when  $\theta \neq \theta_0$ , we have

$$\begin{aligned} F(\theta) &= \frac{e^{j(2\pi N/\varepsilon)(\sin\theta - \sin\theta_0)} - 1}{e^{j(2\pi/\varepsilon)(\sin\theta - \sin\theta_0)} - 1} \\ &= \frac{[e^{j(2\pi N/\varepsilon)(\sin\theta - \sin\theta_0)/2} - e^{-j(2\pi N/\varepsilon)(\sin\theta - \sin\theta_0)/2}]}{[e^{j(2\pi/\varepsilon)(\sin\theta - \sin\theta_0)/2} - e^{-j(2\pi/\varepsilon)(\sin\theta - \sin\theta_0)/2}]} \\ &\cdot \frac{e^{j(2\pi N/\varepsilon)(\sin\theta - \sin\theta_0)/2}}{e^{j(2\pi/\varepsilon)(\sin\theta - \sin\theta_0)/2}} = \frac{e^{j(\pi N/\varepsilon)(\sin\theta - \sin\theta_0)}}{e^{j(\pi/\varepsilon)(\sin\theta - \sin\theta_0)}} \\ &= \frac{\sin((\pi N/\varepsilon)(\sin\theta - \sin\theta_0))}{\sin((\pi/\varepsilon)(\sin\theta - \sin\theta_0))} \\ &= e^{j(\pi/\varepsilon)(N-1)(\sin\theta - \sin\theta_0)} \\ &\cdot \frac{\sin((\pi N/\varepsilon)(\sin\theta - \sin\theta_0))}{\sin((\pi/\varepsilon)(\sin\theta - \sin\theta_0))}. \end{aligned} \quad (\text{A.2})$$

Neglecting the phase factor and normalizing the radiation power, we can obtain the array factor as

$$F(\theta) = \frac{\sin((\pi N/\varepsilon)(\sin\theta - \sin\theta_0))}{N \cdot \sin((\pi/\varepsilon)(\sin\theta - \sin\theta_0))}, \quad (\text{A.3})$$

when  $\theta \neq \theta_0$ .

Let  $F(\theta) = 1$  when  $\theta = \theta_0$ ; then (4) is proved.  $\square$

### B. Obtaining the Lobe Peak Values

Taking the derivative of (5), we have

$$\begin{aligned} \frac{dF(\theta)}{d\theta} &= \begin{cases} 0, & \theta = n\pi, \theta \neq \theta_0 \\ \frac{\pi N}{\varepsilon} \cos\theta \left( \frac{\cos(\sin\theta)}{\sin\theta} - \frac{\sin(\sin\theta)}{\sin^2\theta} \right), & \theta \neq n\pi, \theta \neq \theta_0 \\ 0, & \theta = \theta_0, \end{cases} \quad (\text{B.1}) \end{aligned}$$

where  $n = 0, \pm 1, \pm 2, \dots$ . To obtain the lobe peak values, we can set the above equation to be equal to zero, where the peak values are easily found at  $\hat{\theta}_k = \pm n\pi/2$ . Moreover, from the above equation, the off-boresight angle does not involve the calculation of the peak value.

## Conflict of Interests

The authors declare that there is no conflict of interests regarding the publication of this paper.

## Acknowledgments

This research was supported by the MSIP (Ministry of Science, ICT and Future Planning), Korea, under the ITRC (Information Technology Research Center) Support Program (IITP-2015-H8501-15-1019) supervised by the IITP (Institute for Information & Communications Technology Promotion).

## References

- [1] M. R. Andrews, P. P. Mitra, and R. Decarvalho, "Tripling the capacity of wireless communications using electromagnetic polarization," *Nature*, vol. 409, no. 6818, pp. 316–318, 2001.
- [2] K. H. Jeon, X. Su, B. Hui, and K. H. Chang, "Practical and simple wireless channel models for use in multipolarized antenna systems," *International Journal of Antennas and Propagation*, vol. 2014, Article ID 619304, 10 pages, 2014.
- [3] A. S. Poon and D. N. Tse, "Degree-of-freedom gain from using polarimetric antenna elements," *IEEE Transactions on Information Theory*, vol. 57, no. 9, pp. 5695–5709, 2011.
- [4] M.-T. Dao, V.-A. Nguyen, Y.-T. Im, S.-O. Park, and G. Yoon, "3D polarized channel modeling and performance comparison of MIMO antenna configurations with different polarizations," *IEEE Transactions on Antennas and Propagation*, vol. 59, no. 7, pp. 2672–2682, 2011.
- [5] X. Su, B. Hui, and K. Chang, "3-D MIMO channel modeling with beamforming analysis for dual-polarized antenna systems," in *Proceedings of the IEEE 78th Vehicular Technology Conference (VTC '13)*, September 2013.
- [6] W. Jeon and S. Y. Chung, "The capacity of wireless channels: a physical approach," in *Proceedings of the IEEE International Symposium on Information Theory (ISIT '13)*, pp. 3045–3049, July 2013.
- [7] B. Friedlander and S. Scherzer, "Beamforming versus transmit diversity in the downlink of a cellular communications system," *IEEE Transactions on Vehicular Technology*, vol. 53, no. 4, pp. 1023–1034, 2004.
- [8] G. J. Foschini and M. J. Gans, "On limits of wireless communications in a fading environment when using multiple antennas," *Wireless Personal Communications*, vol. 6, no. 3, pp. 311–335, 1998.
- [9] W. Liu, "Adaptive wideband beamforming with sensor delay-lines," *International Journal of Signal Processing*, vol. 89, no. 5, pp. 876–882, 2009.
- [10] J. Litva and T. K. Lo, *Digital Beamforming in Wireless Communications*, Artech House, 1st edition, 1996.
- [11] W. Liu and S. Weiss, *Wideband Beamforming: Concepts and Techniques*, John Wiley & Sons, 2nd edition, 2012.
- [12] V. K. Sakarellos, D. Skraparlis, A. D. Panagopoulos, and J. D. Kanellopoulos, "Optimum placement of radio relays in millimeter-wave wireless dual-hop networks," *IEEE Antennas and Propagation Magazine*, vol. 51, no. 2, pp. 190–199, 2009.
- [13] G. Wescom, Just a dipole, <http://radio.n0gw.net/radiol1.pdf>.
- [14] P. Graham, "A discussion of antenna theory," <http://k9erg.tripod.com/theory.htm>.
- [15] T. Taga, "Analysis for mean effective gain of mobile antennas in land mobile radio environments," *IEEE Transactions on Vehicular Technology*, vol. 39, no. 2, pp. 117–131, 1990.
- [16] J.-W. Wu, C.-J. Wang, and C. F. Jou, "Method of suppressing the side lobe of a tapered short leaky wave antenna," *IEEE Antennas and Wireless Propagation Letters*, vol. 8, pp. 1146–1149, 2009.
- [17] S.-H. Yang and J.-F. Kiang, "Adjustment of beamwidth and side-lobe level of large phased-arrays using particle swarm optimization technique," *IEEE Transactions on Antennas and Propagation*, vol. 62, no. 1, pp. 138–144, 2014.
- [18] R. S. Blum, "Limiting case of a lack of rich scattering environment for MIMO radar diversity," *IEEE Signal Processing Letters*, vol. 16, no. 10, pp. 901–904, 2009.
- [19] O. Souihli and T. Ohtsuki, "Benefits of rich scattering in MIMO channels: a graph-theoretical perspective," *IEEE Communications Letters*, vol. 17, no. 1, pp. 23–26, 2013.
- [20] S. Sirianunpiboon, S. D. Howard, and A. R. Calderbank, "Diversity gains across line of sight and rich scattering environments from space-polarization-time codes," in *Proceedings of the IEEE Information Theory Workshop on Information Theory for Wireless Networks (ITW '07)*, pp. 1–5, July 2007.



**Hindawi**

Submit your manuscripts at  
<http://www.hindawi.com>

